

Measurement of ω and ϕ meson production via dimuons at forward rapidity in $p\bar{p}$ collisions at $\sqrt{s} = 13.6$ TeV with ALICE.

Masahiro Oida

Contents

1	Introduction	1
1.1	QCD	1
1.2	Chiral symmetry	2
1.3	NJL model	3
1.4	Quark-Gluon Plasma (QGP)	4
1.5	Heavy Ion collision	5
1.6	Dilepton Measurement[5]	6
1.7	Search for chiral symmetry restoration in QGP	8
1.8	Analysis of pp collision data as a baseline	8
2	Detector setup	10
2.1	Large Hadron Collider (LHC)	10
2.2	A Large Ion Collider Experiment (ALICE)	10
2.2.1	MUON Spectrometer	11
2.2.2	MFT	11
2.2.3	MFT-MUON Track Matching	12
3	Analysis	13
3.1	DataSet	13
3.2	Event selection	13
3.3	Single muon track reconstruction	13
3.4	Single muon selection	13
3.5	Dimuon analysis	14
3.5.1	Dimuon reconstruction	14
3.5.2	Combinatorial background subtraction	14
3.5.3	Peak extraction of $\omega \rightarrow \mu\mu, \phi \rightarrow \mu\mu$	17
3.5.4	Yield calculation of ω, ϕ	18
3.6	Analysis for improving MFT-MCH matching purity	19
3.6.1	MFT-MCH matching χ^2 Optimization	19
3.6.2	Fake Match Track Removal Analysis of MFT-MCH-MID Track using MFT Track η - MCH Track η	22
4	Results and Discussion	27
5	Summary	28
6	Acknowledgements	28

Abstract

The masses of hadrons are theoretically explained to dynamically get their mass through the spontaneous chiral symmetry breaking. Hadrons are composed of quarks and gluons. Quarks and gluons obey quantum chromodynamics (QCD), which leads to confinement phenomena and spontaneous chiral symmetry breaking. Then, when the quarks and gluons reaches an ultra-high temperature and dense state, they undergoes a phase transition from the hadron to the quark-gluon plasma (QGP) state. In the QGP state, quarks deconfinement and it suggest the chiral symmetry restoration. The existence of the QGP has been confirmed by heavy-ion collision. Chiral symmetry restoration phenomenon has been explored via dilepton measurement. However, its phenomena have not yet been clearly unreveal, as they can also be explained by other phenomena such as the broadening of ρ mesons due to high-temperature hadron gas.

Therefore, I aim to explore chiral symmetry restoration via dimuon using ALICE in LHC Run3, and by revealing the transverse momentum dependence of the light vector mesons invariant mass distribution change in PbPb collisions. The Large Hadron Collider (LHC) is the world's largest hadron collider. The ALICE experiment has detectors specialized to QGP research, and high muon particle identification detectors in the forward region. The light vector mesons (ρ, ω, ϕ) are probes of hadron's masses inside QGP due to decay into only dimuons and have short lifetime. The advantage of using muons is that they don't include π^0 Dalitz decays and γ conversion. Therefore it is a better S/N than dielectron measurement. Furthermore, a new silicon detector (MFT) has been installed to the forward region from LHC Run3. It enables accurate measurement of the muon production point and lower transverse momentum than Run2. As a result, it enables removal of muons from heavy flavor using lifetime differences. Also the accuracy of the pseudorapidity and azimuth angle measurement of muons improves the mass resolution.

This thesis shows the transverse momentum dependence of ω and ϕ mesons invariant mass using forward dimuons in $\sqrt{s} = 13.6$ TeV pp collisions with ALICE, as a step toward measuring the modified in the invariant mass distribution of light vector mesons induced by QGP. The dimuon invariant mass was calculated using track reconstruction with forward region detectors, including MFT. A fit was performed on the ω and ϕ peak extracted from it and the yield was calculated. Along with this analysis, the matching χ^2 between the MFT and its backward detector, the MCH track, was optimised. Concerning the matching of MFT and MCH tracks, a removal analysis of incorrectly matched tracks was also carried out. It is shown that a cut applied to the pseudorapidity difference between MFT and MCH tracks, formed using all forward detectors, can remove incorrectly matched tracks.

1 Introduction

1.1 QCD

The fundamental components of the matter around us are elementary particles. The behaviour of elementary particles, such as quarks and gluons, is described by quantum field theory. In particular, quarks and gluons possess degrees of freedom called "color," the physics governing this degree of freedom is known as Quantum Chromodynamics (QCD). QCD is based on an SU(3) gauge theory and describes the strong interaction. The QCD Lagrangian is expressed as follows:

$$\mathcal{L}_{QCD} = \sum_q \bar{\psi}_{q,a} (i\gamma^\mu \partial_\mu - m_q) \psi_{q,a} + g_s \sum_q \bar{\psi}_{q,a} \gamma^\mu T^A_{ab} \psi_{q,b} G_\mu^A - \frac{1}{4} G_\mu^A G^{A\mu\nu} \quad (1)$$

$\psi_{q,a}$ and $\bar{\psi}_q q, a$ represent the quark and antiquark fields, where q denotes the flavor degree of freedom, and a denotes the color degree of freedom. γ^μ is the gamma matrices, m_q is the particle mass corresponding to each flavor, g_s is the QCD coupling constant, $T^A * ab$ are the generator matrices, G_μ^A is the gluon field, and $G_{\mu\nu}^A$ is the gluon field tensor.

The first term in (1) represents the term for a free particle of mass m , the second term represents the interaction between quarks and gluons, and the third term represents the interaction between gluons themselves. A significant difference from Quantum Electrodynamics (QED), which describes electromagnetic interactions, is the presence of the coupling constant $\alpha_s(Q^2)$ and the self-interaction of the gluon field. In QED, the coupling constant does not depend on the energy scale. However, the coupling constant $\alpha_s(Q^2)$ that appears in QCD depends on the energy scale. Figure 1 shows how the coupling con-

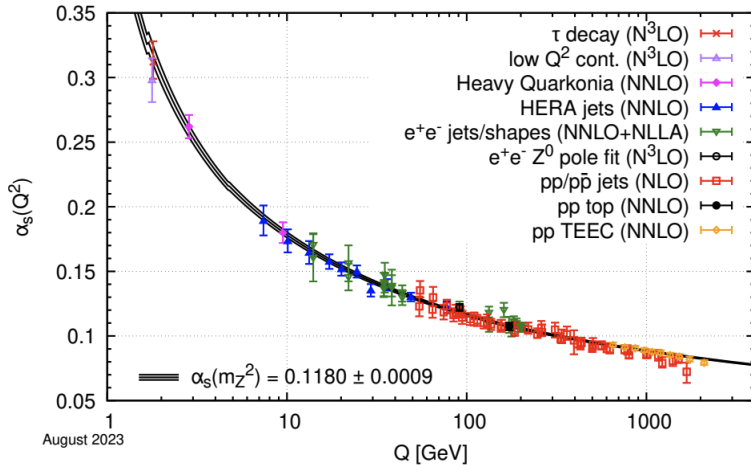


Figure 1: QCD coupling constant[1]

stant $\alpha_s(Q^2)$ changes with the energy scale. The coupling constant becomes small at high energy scales, corresponding to short distances. This reflects the phenomenon of asymptotic freedom, where quarks behave as free particles when they are sufficiently close to each other. On the other hand, at low energy scales corresponding to long distances, the coupling constant grows infinitely large. This represents the phenomenon of quark confinement, where quarks cannot be isolated as individual particles.

Next, I describe the self-interaction of gluons. The gluon field tensor is expressed as:

$$G_{\mu\nu}^A = \partial_\mu G_\nu^A - \partial_\nu G_\mu^A + g_s f^{ABC} G_\mu^B G_\nu^C \quad (2)$$

where f^{ABC} are the structure constants of the SU(3) group. Substituting this into the third term of (1),

we obtain:

$$\begin{aligned} -\frac{1}{4}G_{\mu\nu}^A G^{A\mu\nu} &= -\frac{1}{4}(\partial_\mu G_\nu^A - \partial_\nu G_\mu^A + g_s f^{ABC} G_\mu^B G_\nu^C)(\partial^\mu G^{A\nu} - \partial^\nu G^{A\mu} + g_s f^{ABC} G^{B\mu} G^{C\nu}) \\ &= -\frac{1}{4}(\partial_\mu G_\nu^A - \partial_\nu G_\mu^A)(\partial^\mu G^{A\nu} - \partial^\nu G^{A\mu}) \\ &\quad - g_s f^{ABC} G_\mu^B G_\nu^C \partial^\mu G^{A\nu} - g_s^2 f^{ABE} f^{CDE} G_\mu^A G_\nu^B G^{C\mu} G^{D\nu} \end{aligned} \quad (3)$$

In (3), the first term represents the free gluon field without interactions. The second term represents interactions involving three gluon fields, representing reactions such as $g + g \rightarrow g$. The third term corresponds to interactions involving four gluon fields, representing reactions such as $g + g \rightarrow g + g$. For photons, the third term in (2) does not exist, so the second and third terms in (3) do not appear. This is because gluons interact with each other due to their color degrees of freedom, which gives rise to gluon self-interaction.

These characteristics—namely, the energy dependence of the coupling constant and the self-interaction of gluons—contribute to the complex structure of the quark-gluon interactions.

1.2 Chiral symmetry

The quark field can be separated into its right-handed and left-handed components. The projection operators for the right-handed and left-handed components are defined as P_R and P_L , respectively. Using the γ matrices, they are expressed as follows:

$$P_R = \frac{1 + \gamma_5}{2}, \quad P_L = \frac{1 - \gamma_5}{2} \quad (4)$$

The following equations hold for these projection operators.

$$P_R + P_L = 1, \quad P_R P_L = 0, \quad P_R^2 = P_R, \quad P_L^2 = P_L \quad (5)$$

The right-handed quark field q_R and the left-handed quark field q_L are expressed using the projection operators as follows:

$$q_R = P_R q, \quad q_L = P_L q \quad (6)$$

These components are applied to the QCD Lagrangian:

$$\mathcal{L}_{QCD} = \sum_q \bar{q}(i\gamma^\mu D_\mu - m)q \quad (7)$$

- Kinetic Term (First Term of the QCD Lagrangian)

$$\bar{q}(i\gamma^\mu D_\mu)q = \bar{q}(i\gamma^\mu D_\mu)(P_R^2 + P_L^2)q \quad (8)$$

$$= \bar{q}P_L(i\gamma^\mu D_\mu)P_R q + \bar{q}P_R(i\gamma^\mu D_\mu)P_L q \quad (9)$$

$$= \bar{q}_R(i\gamma^\mu D_\mu)q_R + \bar{q}_L(i\gamma^\mu D_\mu)q_L \quad (10)$$

- Mass Term (Second Term of the QCD Lagrangian)

$$\bar{q}m q = \bar{q}m(P_R^2 + P_L^2)q \quad (11)$$

$$= \bar{q}P_R m P_R q + \bar{q}P_L m P_L q \quad (12)$$

$$= \bar{q}_L m q_R + \bar{q}_R m q_L \quad (13)$$

From the above, the kinetic term of the quark field can be separated into the right-handed and left-handed quark fields, thereby preserving chiral symmetry. However, the mass term mixes the right-handed

and left-handed quark fields, breaking chiral symmetry. Considering the chiral limit ($m_q = 0$), the QCD Lagrangian preserves chiral symmetry.

The order parameter for the spontaneous breaking of chiral symmetry is represented by the quark condensate $\langle \bar{q}q \rangle$. As shown in Figure 2, this quantity takes a finite value in the ground state of hadrons at standard temperature and density. But, it is expected to approach $\langle \bar{q}q \rangle \sim 0$ at extremely high temperatures and densities.

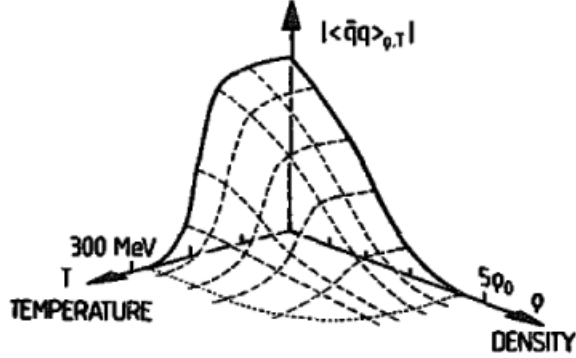


Figure 2: Quark condensate[2]

Since the vacuum expectation value of the quark condensate cannot be directly measured, as described later, various other probes are used to investigate the restoration of chiral symmetry.

1.3 NJL model

The interaction between quarks and gluons, as described in 1.1, exhibits a complex structure, making it difficult to understand various phenomena from first-principle calculations. Therefore, models are employed to describe various phenomena. One such model is the Nambu-Jona-Lasinio (NJL) model, a chiral effective model. Its Lagrangian is expressed as follows:

$$\mathcal{L} = \bar{q}i\gamma \cdot \partial q - (-g)[(\bar{q}q)^2 + (\bar{q}i\gamma_5 q)^2] \quad (14)$$

where, q and \bar{q} represent quark and antiquark fields, respectively; γ and γ_5 are gamma matrices, with $\gamma_5 = i\gamma_0\gamma_1\gamma_2\gamma_3$. Since there is an attractive force between quarks and antiquarks, the coupling constant g is positive and has a dimension of [mass] $^{-2}$. This model serves as a chiral effective theory for QCD at the energy scale of 1 GeV. To determine the ground state of this Lagrangian, the self-consistent mean field approximation (MFA) is employed:

$$\langle \bar{q}q \rangle \equiv \frac{-m_0^2\sigma}{G} \quad (15)$$

$$\langle \bar{q}i\gamma_5 q \rangle \equiv \frac{-m_0^2\pi}{G} \quad (16)$$

By substituting (15) and (16) into (14), the expression is reformulated. Defining $\sigma = \bar{q}q$, $\pi = \bar{q}i\gamma_5 q$, and $2g = (G/m_0)^2$, we get:

$$\mathcal{L}_{MFA} = \bar{q}[i\gamma \cdot \partial - G(\sigma + i\pi\gamma_5)]q - \frac{m_0^2}{2}(\sigma^2 + \pi^2) \quad (17)$$

where, defining $q_\theta = e^{i\gamma_5 \frac{\theta}{2}} q$, $G\sqrt{\sigma^2 + \pi^2} = M$, and $\pi/\sigma = \tan\theta$, the Hamiltonian can be expressed as follows. θ is the parameter of the chiral transformation.

$$H_{MFA} = \int d^3x \left\{ \bar{q}_\theta(x)(-i\gamma \cdot \nabla + M)q_\theta(x) + \frac{m_0^2}{2}\sigma_0^2 \right\} \quad (18)$$

where $\sigma_0^2 = \sigma^2 + \pi^2$. Since π is considered sufficiently small, we write σ to σ_0 . From this Hamiltonian, the Dirac equation for mass M can be derived. Its solution is given as:

$$q_\theta(x) = \frac{1}{\sqrt{V}} \sum_{\mathbf{p}, r=\pm} \sqrt{\frac{M}{E_p}} \left\{ a_M(\mathbf{p}, r) u_M(\mathbf{p}, r) e^{-ip \cdot x} + b_M^\dagger(\mathbf{p}, r) v_M(\mathbf{p}, r) e^{ip \cdot x} \right\} \quad (19)$$

where, r represents helicity, $E_p = \sqrt{\mathbf{p}^2 + M^2}$, and $M = -g \langle \bar{q}_\theta q_\theta \rangle$. Next, when $q_\theta(x)$ is expanded using spinors with zero mass, the solution is:

$$q_\theta(x) = \frac{1}{\sqrt{V}} \sum_{\mathbf{p}, s=R,L} \left\{ a_{\mathbf{p}}^{(s)}(t) u_0(\mathbf{p}, s) e^{-i\mathbf{p} \cdot \mathbf{x}} + b_{\mathbf{p}}^{(s)\dagger}(t) v_0(\mathbf{p}, s) e^{i\mathbf{p} \cdot \mathbf{x}} \right\} \quad (20)$$

where s represents helicity. Using the solutions (19) and (20), the Hamiltonian (18) can be expressed in terms of operators for massive and massless states. Here, $a_{\mathbf{p}}$ and $b_{\mathbf{p}}$ are expansion coefficients:

$$\begin{aligned} H_{MFA} &= \sum_{\mathbf{p}, s} \left\{ |\mathbf{p}| \left(a_{\mathbf{p}}^{(s)\dagger}(t) a_{\mathbf{p}}^{(s)}(t) - b_{-\mathbf{p}}^{(s)}(t) b_{-\mathbf{p}}^{(s)\dagger}(t) \right) \right\} \\ &\quad + M \left(b_{-\mathbf{p}}^{(s)}(t) a_{\mathbf{p}}^{(s)}(t) + a_{\mathbf{p}}^{(s)\dagger}(t) b_{-\mathbf{p}}^{(s)\dagger}(t) \right) + V \frac{m_0^2}{2} \sigma_0^2 \end{aligned} \quad (21)$$

$$= \sum_{\mathbf{p}, r} E_p \left(a_M^\dagger(\mathbf{p}, r) a_M(\mathbf{p}, r) - b_M^\dagger(\mathbf{p}, r) b_M(\mathbf{p}, r) \right) + V \frac{m_0^2}{2} \sigma_0^2 \quad (22)$$

From this Hamiltonian, the following Heisenberg equation can be derived:

$$i \begin{pmatrix} \dot{a}_{\mathbf{p}}^{(s)}(t) \\ \dot{b}_{-\mathbf{p}}^{(s)}(t) \end{pmatrix} = \begin{pmatrix} |\mathbf{p}| & M \\ M & -|\mathbf{p}| \end{pmatrix} \begin{pmatrix} a_{\mathbf{p}}^{(s)}(t) \\ b_{-\mathbf{p}}^{(s)}(t) \end{pmatrix} \quad (23)$$

Setting the initial state $a_{\mathbf{p}}^{(s)}(t=0) = a_{M=0}(\mathbf{p}, s)$, the solution reveals that the massive and massless operators are connected via the Bogoliubov transformation:

$$\begin{pmatrix} a_M(\mathbf{p}, r) \\ b_M(\mathbf{p}, r)^\dagger \end{pmatrix} = U(\mathbf{p}, r) \begin{pmatrix} a_0(\mathbf{p}, r) \\ b_0(\mathbf{p}, r)^\dagger \end{pmatrix} U^\dagger(\mathbf{p}, r) \quad (24)$$

where $U(\mathbf{p}, r) = \exp \left\{ -\frac{\theta_p}{2} (a_0^\dagger(\mathbf{p}, r) b_0^\dagger(-\mathbf{p}, r) - b_0(-\mathbf{p}, r) a_0(\mathbf{p}, r)) \right\}$. The vacuum states for each operator are defined as follows:

$$|\sigma_0\rangle \rightarrow a_M(\mathbf{p}, r) |\sigma_0\rangle = b_M(\mathbf{p}, r) |\sigma_0\rangle = 0 \quad (25)$$

$$|0\rangle \rightarrow a_0(\mathbf{p}, r) |0\rangle = b_0(\mathbf{p}, r) |0\rangle = 0 \quad (26)$$

$a_0(\mathbf{p}, r)^\dagger$ creates an eigenstate of chirality, while $a_M(\mathbf{p}, r)^\dagger$ creates an eigenstate of helicity. Based on the vacuum definition and (24), acting on $|0\rangle$ produces an eigenstate of helicity but not a definite chirality eigenstate. This implies that "chiral symmetry is spontaneously broken".

Thus, the NJL model theoretically predicts vacuum phase transitions. In our universe, it is believed that quark condensation spontaneously breaks chiral symmetry, leading to hadrons acquiring significant masses.

1.4 Quark-Gluon Plasma (QGP)

When hadrons are exposed to extremely high temperatures and densities, they transition into a plasma state known as the Quark-Gluon Plasma (QGP). In the QGP state, quarks are resolved from confinement, and the restoration of chiral symmetry is also expected. Furthermore, it is believed that the universe immediately following the Big Bang was in a QGP state. On the QCD phase diagram, which represents the phase structure of quarks and gluons, the QGP phase appears as shown in Figure 3.

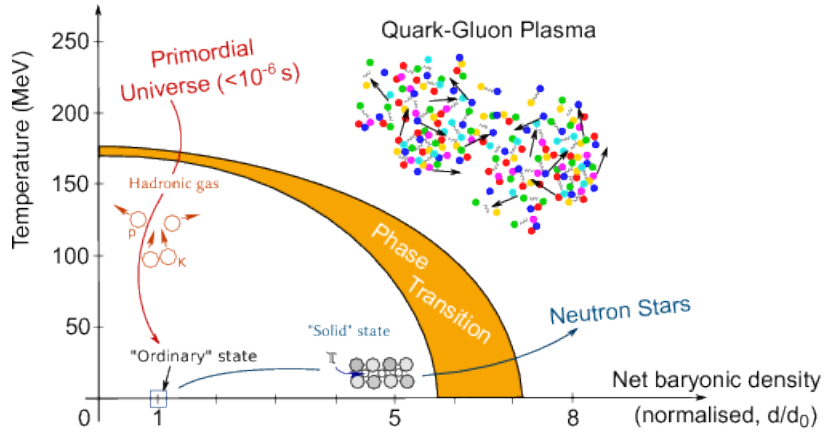


Figure 3: QCD Phase Diagram[3]

The QGP phase can be observed in high-temperature regions in both high-density and low-density areas. Two types of phase transitions are related in the transition to the QGP phase. The first is the chiral phase transition. The second is the deconfinement-confinement phase transition.

The chiral phase transition is the spontaneous breaking of chiral symmetry as the vacuum undergoes a phase transition, allowing quarks to acquire a substantial effective mass. In other words, the chiral phase transition is deeply related to the mass acquisition of hadrons. The deconfinement-confinement phase transition pertains to the confinement of quarks. In the hadronic ground state, quarks are confined by color interaction. However, in the QGP state, quarks are resolved from confinement and transition into a plasma state. This is the deconfinement-confinement phase transition. While these transitions are believed to occur at approximately a similar critical temperature, this relationship is not self-evident, and research is still ongoing.

1.5 Heavy Ion collision

The existence of QGP, which are ultrahigh-temperature or dense materials, has been confirmed by heavy-ion collision experiments. As shown in Figure 4, the time evolution proceeds in the following.

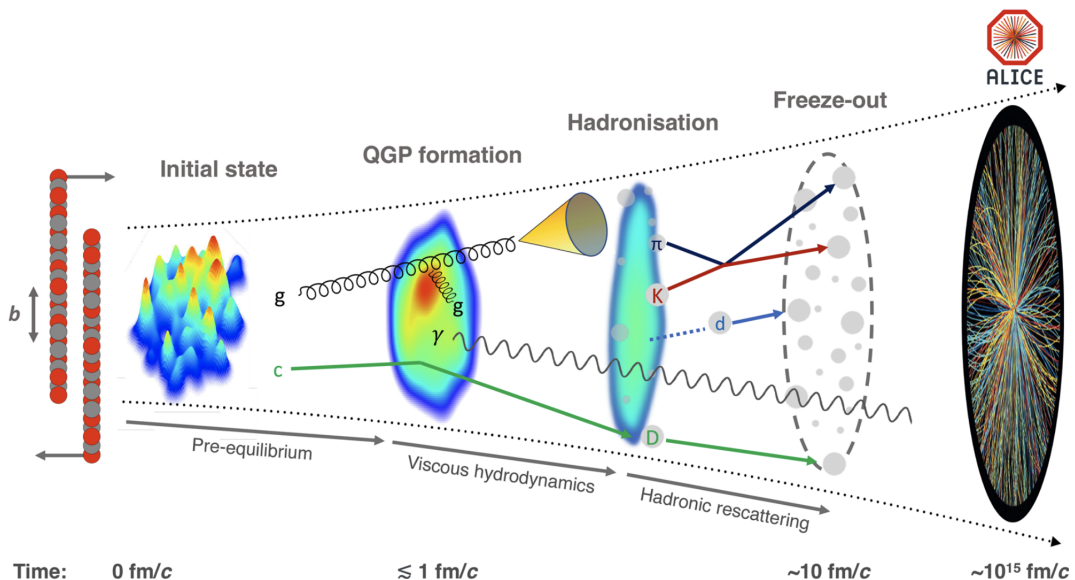


Figure 4: The evolution of a heavy-ion collision at LHC energies[4]

-
1. Pre-equilibrium state
 2. QGP
 3. Hadronization
 4. Kinetic Freeze-out

In the initial stage of the collision, partons from the nucleons undergo elastic and deep inelastic scatterings to reach thermalization. During this initial collision, phenomena such as jet production and the pair production of heavy quarks occur. Once the material generated in the collision region reaches thermal equilibrium, the system transitions into the QGP state.

In the QGP state, photons and lepton pairs originating from the thermal radiation of high-temperature matter are generated. Jets interact with the QGP and lose energy, resulting in jet quenching, while heavy quarks undergo deconfinement due to the color Debye screening. Subsequently, as the QGP cools, hadronization occurs, leading to chemical freeze-out.

Chemical freeze-out refers to the stop of changes in particle species due to deeply inelastic scatterings among particles. However, elastic scatterings between hadrons continue, and momentum exchange among particles. Later, kinetic freeze-out occurs, fixing the momenta and other properties of the particles. The particles finally detected are those that remain after the kinetic freeze-out. Thus, QGP is formed during the temporal evolution of heavy-ion collisions, and its lifetime is extremely short.

The QGP generated in heavy-ion collisions has its density and temperature determined by the collision energy. High-density QGP regions are realized at collision energies of $\sqrt{s_{NN}} \lesssim 10$ [GeV]. At these energies, the colliding particles stop at the collision point. They create a high-density state where kinetic energy is converted directly into heat, increasing the temperature.

On the other hand, high-temperature, low-density regions are achieved at collision energies of $\sqrt{s_{NN}} \gtrsim 100$ [GeV]. In this energy regime, the colliding particles do not stop but pass through each other, producing a large number of pair creation. As a result, the baryon number density does not become large relative to the temperature. However, a high energy density region leads to the creation of high-temperature matter near the collision point.

In the ALICE experiment, LHC Run 3 operations began in 2022, initiating Pb-Pb collision measurements at $\sqrt{s_{NN}} = 5.36$ TeV. This collision energy produces QGP in the ultrahigh temperature, low-density region. Moreover, compared to the QGP generated at $\sqrt{s_{NN}} = 200$ GeV at RHIC, the higher collision energy at LHC enables the measurement of a larger QGP than ever before.

1.6 Dilepton Measurement[5]

Dilepton measurement is a good probe to investigate the time evolution of heavy-ion collisions. Leptons do not interact with strong interactions, making them less affected by the QGP. This characteristic allows for the measurement of a distribution that sums up dileptons from all stages of heavy-ion collisions. The sources of dilepton production are as follows:

- Primordial dileptons (from $q\bar{q}$ annihilation)
- Thermal dileptons
- Dileptons from hadron decays

The dilepton mass regions are associated with the time evolution of heavy ion collisions respectively.

In the High-Mass Region, primordial dileptons (Drell-Yan) constitute the continuum component of the mass distribution. It is related to the initial state of the collision. In the Intermediate-Mass Region, thermal dileptons originating from the QGP and continuum components such as open-charm and open-beauty are observed.

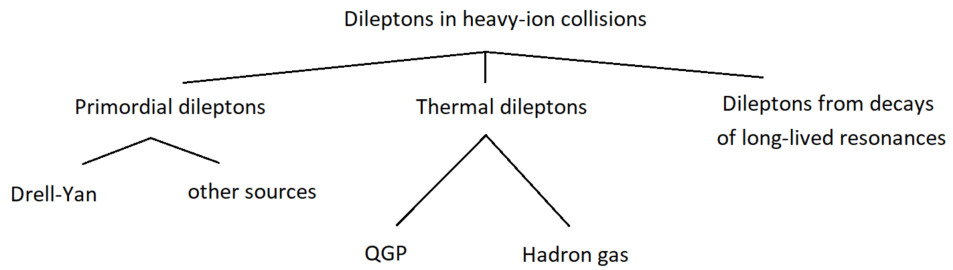


Figure 5: Dilepton source

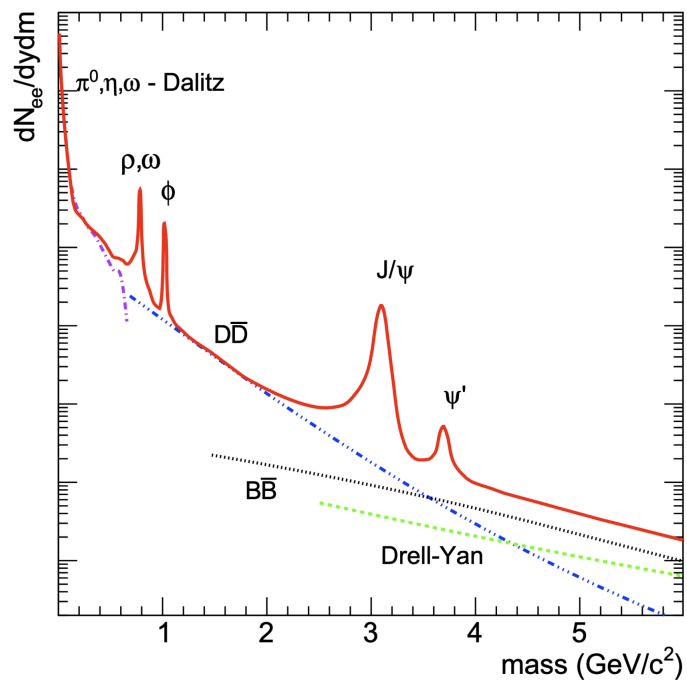


Figure 6: Expected mass spectrum from dileptons[7]

Finally, in the Low-Mass Region, the dilepton distribution is predominantly derived from light meson decays from the hadronic gas. Most dileptons from hadron decays have longer lifetimes compared to the QGP. So these mesons observed in this region are mostly from the hadron gas. However, light vector mesons (ρ, ω, ϕ) have extremely short lifetimes. They may be affected by QGP.

1.7 Search for chiral symmetry restoration in QGP

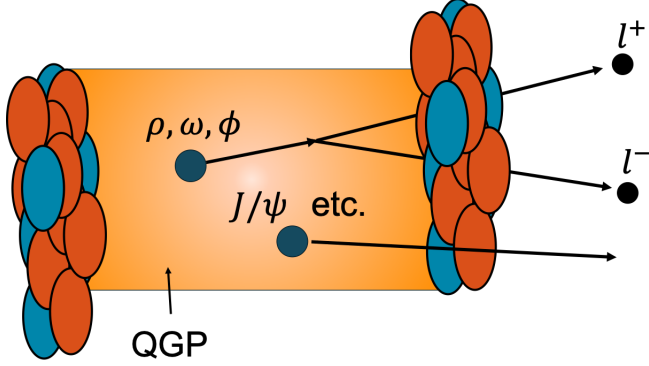


Figure 7: Low mass vector meson decay in QGP

In the QGP, it is expected that an ultra-high temperature and high-density state is realized, leading to $<\bar{q}q> \sim 0$ and the restoration of chiral symmetry. Light vector mesons (ρ, ω, ϕ) serve as probes for the masses of hadrons in the QGP. These particles have short lifetimes and decay channels into dileptons. As shown in Fig.4, their short lifetimes make it possible for them to decay within the QGP, which would otherwise immediately hadronize. Additionally, since they decay exclusively into dileptons, which do not undergo strong interactions with the QGP, the masses of hadrons within the QGP can be measured.

In past experiments, the restoration of chiral symmetry was investigated using dileptons. In the SPS-NA60 experiment, the excess of muon pairs in the low-mass region was reported. However, the excess could also be explained by $\pi + \pi \rightarrow \rho \rightarrow \pi\pi$, and thus it did not serve as definitive evidence of chiral symmetry restoration[8].

Additionally, in the electron pair measurements during ALICE Run 2 $\sqrt{s_{NN}} = 5.02$ TeV PbPb collisions, contributions from open-charm and open-beauty were estimated along with the vacuum dilepton distribution excluding ρ , and an excess of electron pairs was reported. The excess was explained as thermal dileptons from the QGP within the error range demonstrated[6].

This study aims to measure the mass modification of light vector mesons in the QGP using forward muon pairs in ALICE Run 3 $\sqrt{s_{NN}} = 5.36$ TeV PbPb collisions. Starting from ALICE Run 3, the MFT was introduced into the forward detector system of the ALICE experiment. It enables more precise measurements of muon production points compared to Run 2, as well as measurements of muons with lower transverse momentum. By utilizing the differences in muon production points of heavy flavor (HF), which is one of the backgrounds in light vector meson measurements, can be removed. This will allow the precise measurement of the mass distribution of low transverse momentum light vector mesons, which are more likely to decay within the QGP.

1.8 Analysis of pp collision data as a baseline

This paper presents the analysis results of proton-proton collision events. The particles generated in proton-proton collisions are produced from the vacuum. Measurements of collision events where QGP is not produced serve as a baseline for comparison with events where QGP is generated. Currently, the quality of track reconstruction is still insufficient, and the muon pair analysis is also incomplete.

Furthermore, the quality of muon tracks in heavy-ion collisions is more challenging than in proton-proton collisions due to the large number of particles generated in each event.

The purpose of this study is to provide an analysis as a baseline for future studies of $\sqrt{s_{NN}} = 5.02$ PbPb collisions, where QGP is expected to be generated and to improve the quality of muon tracks in ALICE Run 3 $\sqrt{s_{NN}} = 13.6$ TeV pp collisions.

2 Detector setup

2.1 Large Hadron Collider (LHC)

The Large Hadron Collider (LHC) is the world's largest circular accelerator. As shown in Figure 8, the LHC and its major experimental groups are located near Geneva, Switzerland. LHC Run 1 was conducted from 2009 to 2013, and Run 2 took place from 2015 to 2018. The ongoing Run 3 is scheduled to collect physics data from 2022 to the summer of 2026. During the run, most of the periods involve proton-proton collision measurements, with heavy-ion collision measurements conducted for about one month each year. The LHC accelerator hosts four major experimental groups: ATLAS, CMS, LHCb, and ALICE.

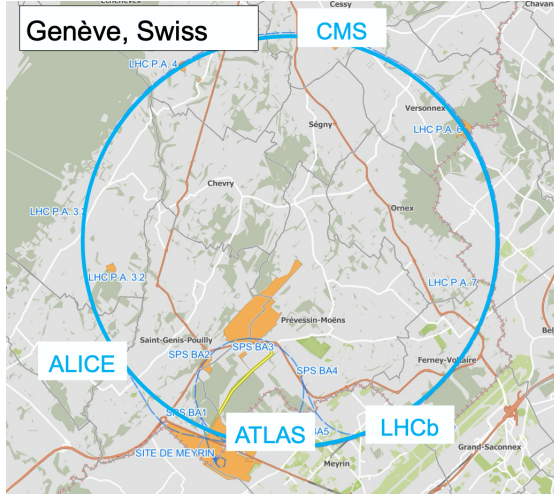


Figure 8: LHC

2.2 A Large Ion Collider Experiment (ALICE)

The ALICE collaboration is an international collaboration consisting of 168 research institutions from 40 countries and around 2,000 researchers. The ALICE detector system is dedicated to research related to the Quark-Gluon Plasma (QGP) produced in heavy-ion collisions. The detectors can be broadly

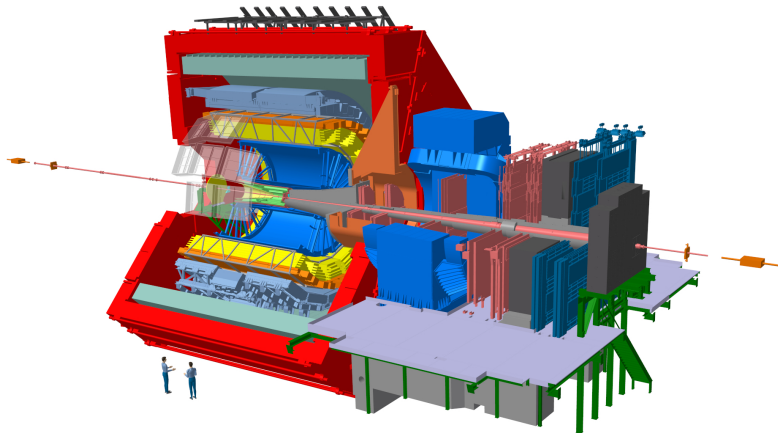


Figure 9: ALICE detectors

divided into two main groups: the barrel detector group and the forward detector group. The barrel detector group includes detectors such as ITS, TPC, TOF, EMCal, TRD, PHOS/CPV, and HMPID.

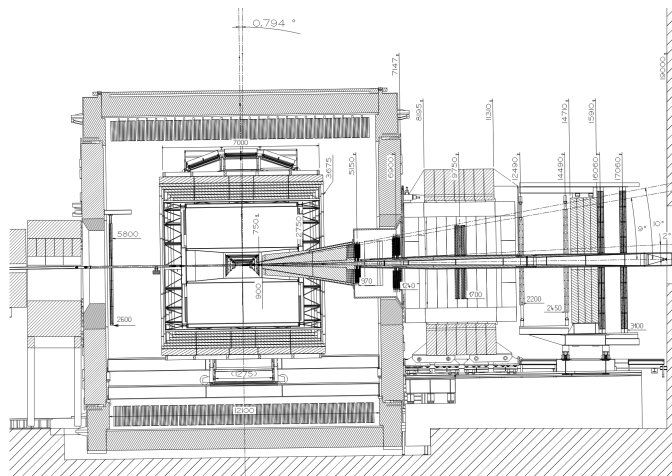


Figure 10: MUON spectrometer

A magnetic field is applied along the beam axis, bending the motion of charged particles and enabling particle identification, momentum, and energy measurements. The forward detector group is specifically designed for muon measurements and consists of three trackers—MFT, MCH, and MID—and two hadron absorbers. A dipole magnet is placed between MCH, allowing the measurement of muon momentum and sign. Other detectors include ZDC and FIT. The ZDC is placed far forward from the collision point and measures the number of neutrons and protons, determining the centrality of heavy-ion collision events. The FIT detectors are placed both forward and backward and are used for measuring event luminosity and particle multiplicity.

2.2.1 MUON Spectrometer

The MUON spectrometer consists of the Front Absorber, MCH, Iron Wall, and MID, and has an acceptance range of $-4.0 < \eta < -2.5$. It uses the high penetration power of muons to identify them. Various particles generated at the collision point (IP) pass through the Front Absorber. Hadrons and light electrons, which interact strongly, are absorbed by the Front Absorber. The muons pass through it due to their high penetration power. The muons that pass through the Front Absorber are detected, and any particles such as π mesons that are produced from interactions within the Front Absorber are measured by the MCH. These particles are then absorbed in the Iron Wall, so they are not detected by the MID. Therefore, muon identification (PID) is performed by combining tracks measured in the MCH and MID. The momentum of the muons is measured using a dipole magnet in the MCH, which is set at a magnetic flux density of 3.0T.

2.2.2 MFT

The MFT is a newly introduced silicon pixel detector in Run 3, installed between $z = 0$ and $z = -76.8$ cm (with an acceptance range of $-3.6 < \eta < -2.5$). It consists of 5 layers of disks that detect tracks and reconstruct MFT standalone tracks considering the influence of the L3 magnet, which creates the ALICE central magnetic field. Since the detector is placed in front of the Front Absorber, the tracks measured include not only muons but also various other particles such as π mesons and kaons. By combining these tracks with those measured by the backward MUON spectrometer, it is possible to measure the DCA of the muons. The ability to measure DCA enables the separation of c and b quarks based on differences in lifetime. Additionally, the precision of the opening angle of the muon pair is improved, which enhances mass resolution. Furthermore, since the MFT is placed in front of the Front Absorber, it allows for the measurement of lower transverse momentum muons compared to those measured by the

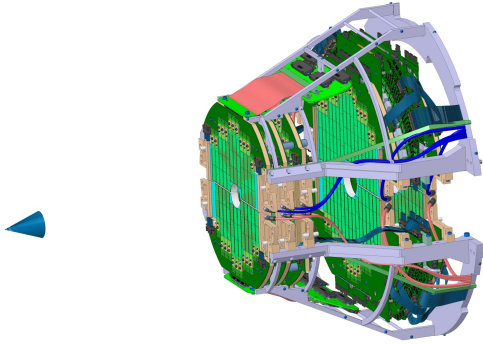


Figure 11: MFT

MUON spectrometer alone.

2.2.3 MFT-MUON Track Matching

The tracks measured by the MUON spectrometer and MFT are matched to reconstruct the Global Track. First, the tracks measured by the MUON spectrometer are extrapolated toward the collision point up to the last disk of the MFT, located at $z = 76.8$ cm. The extrapolation accounts for multiple scattering and energy loss corrections in the hadron absorber between the MUON spectrometer and MFT. Then, suitable MFT tracks are selected based on both position and direction, and the matching quality is evaluated by comparing the position and slope of the tracks. The best quality MFT track is selected and used to construct the Global Track.

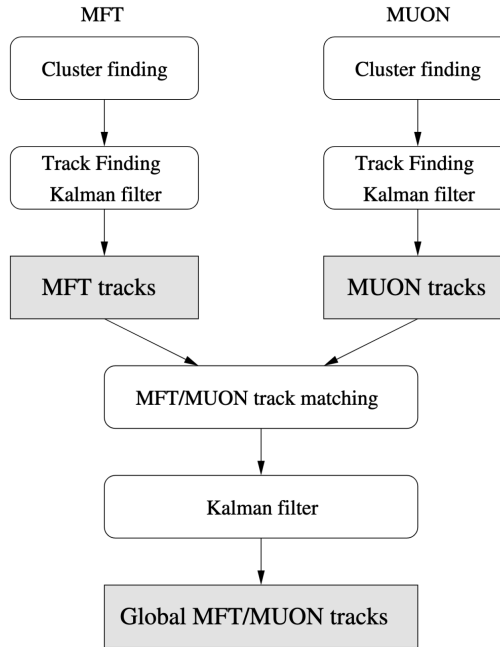


Figure 12: Global Track[9]

3 Analysis

3.1 DataSet

The data used is a part of pp collisions at $\sqrt{s} = 13.6$ TeV obtained in 2022. The collision rate of pp is 500 kHz, and the dataset name is LHC22o_apass7. The Monte Carlo simulation data used in 3.6.2 utilized Pythia8 Monash to reproduce 500 kHz pp collisions at $\sqrt{s} = 13.6$ TeV, employing minimum bias event simulations without extracting specific events.

3.2 Event selection

The position of the proton-proton collision was measured by the ITS detector system. The Z-coordinate of the collision point, denoted as $VtxZ$, was selected with the condition $|VtxZ| < 10$ cm, using the ITS center at $Z = 0$ as the reference. This cut value is aligned with the ITS acceptance. The number of events obtained with this cut is 5.5×10^9 .

3.3 Single muon track reconstruction

As described in 2.2.3, the reconstructed Global Track was used to calculate various physical quantities of the muon as follows: The muon's η and ϕ were calculated using the MFT standalone Track. The momentum p was derived by propagating the MCH standalone track to the Z-coordinate of the collision point, with corrections applied for multiple scattering and energy loss in the absorber. For the DCA, a Global Fit was performed for all tracks constituting the Global Track, and the resulting track was used. As shown in Fig. 13, the track was linearly extrapolated to the Z-coordinate of the collision point (IP), and the distance between the extrapolated point and the collision point was calculated as the DCA. Similarly, using the same track, R_{abs} was calculated as the distance from the beam axis at the back edge of the absorber, as shown in Fig. 14. Furthermore, the MFT-MCH matching χ^2 was calculated based on the parameter differences when extrapolating the MFT track and MCH track to the matching plane.

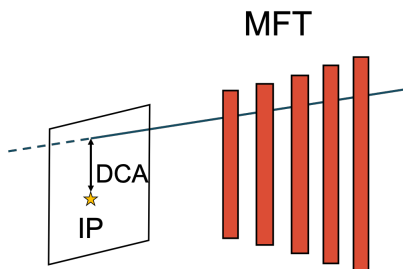


Figure 13: conceptual scheme of DCA

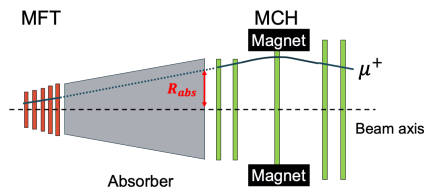


Figure 14: conceptual scheme of R_{abs}

3.4 Single muon selection

The cuts applied to the obtained muon tracks are as follows:

- $-3.6 < \eta < -2.5$
- $17.5 \text{ cm} < R_{abs} < 89.5 \text{ cm}$
- $pDCA < 6\sigma$
- MFT-MCH matching $\chi^2 < 30$

The η cut is aligned with the MFT-MHC-MID acceptance. The R_{abs} cut value is set to exclude values that are influenced by the presence of the hadron absorber rear end. The $pDCA$ is the product of momentum and DCA , and this cut is applied to remove muons originating from beam gas. Tracks with $pDCA$ larger than 6σ when fitted with a Gaussian distribution are excluded. The final MFT-MCH matching χ^2 value is obtained from a fit using the detected points of the MFT and MCH tracks when matching them. The value used in this study is optimized, as described later, to maximize the statistical uncertainty of the yields for ω and ϕ .

3.5 Dimuon analysis

3.5.1 Dimuon reconstruction

Using the single muons selected in 3.4, dimuons are reconstructed. The mass($M_{\mu\mu}$), transverse momentum(p_T), pseudorapidity(η), and Azimuth angle(ϕ) of the dimuon are calculated as (28) (34). First, the p_T , η , and ϕ of the single muons are converted into four-component vectors (p_x, p_y, p_z, E) using (28),(29),(30),(30).

$$p_x = p_T \cos(\phi) \quad (27)$$

$$p_y = p_T \sin(\phi) \quad (28)$$

$$p_z = p_T \sinh(\eta) \quad (29)$$

$$E = \sqrt{p_T^2 \cosh^2(\eta) + m_\mu^2} \quad (30)$$

Then, using the (p_x, p_y, p_z, E) of the single muons, the $(P_x, P_y, P_z, E_{\mu\mu})$ of the dimuon are calculated.

$$\begin{pmatrix} P_x \\ P_y \\ P_z \\ E \end{pmatrix} = \begin{pmatrix} p_{x1} \\ p_{y1} \\ p_{z1} \\ E_1 \end{pmatrix} + \begin{pmatrix} p_{x2} \\ p_{y2} \\ p_{z2} \\ E_2 \end{pmatrix} \quad (31)$$

Using the obtained four-component vector of the dimuon $(P_x, P_y, P_z, E_{\mu\mu})$, the pair's $M_{\mu\mu}$, p_T , and η were calculated from the (33),(34),(34).

$$M_{\mu\mu} = \sqrt{E^2 - (p_x^2 + p_y^2 + p_z^2)} \quad (32)$$

$$p_{T\mu\mu} = \sqrt{p_x^2 + p_y^2} \quad (33)$$

$$\eta_{\mu\mu} = -\log \left(\tan \left(\frac{1}{2} \arctan \left(\frac{\sqrt{p_x^2 + p_y^2}}{p_z} \right) \right) \right) \quad (34)$$

Using the above formulas, the physical quantities of the dimuon are calculated.

3.5.2 Combinatorial background subtraction

The dimuon was reconstructed by pairing oppositely charged muons present in each event. In cases where there are multiple combinations, all combinations are used to pair the muons and reconstruct the physical quantities of the dimuon. Since all combinations are considered, the mass distribution of uncorrelated muon pairs is also reconstructed. This is called the combinatorial background. In this study, the Like Sign method is used to subtract the combinatorial background. The Like Sign method is a method that estimates the combinatorial background by using the mass distribution of muon pairs with the same sign from each collision event. The key feature of this method is that it estimates the shape of uncorrelated background events using the like-sign muons from the same event, allowing for the subtraction of mass distributions of weakly correlated particles within each event, such as those arising from elliptic flow in heavy-ion collisions. The estimated uncorrelated background events depend on the p_T of the dimuon.

The calculation formula is given by (35).

$$\frac{dN_{sig}}{dm} = \frac{dN_{same}^{+-}}{dm} - 2R \sqrt{\frac{dN_{same}^{++}}{dm} \frac{dN_{same}^{--}}{dm}} \quad (35)$$

$$2R = \frac{\frac{dN_{mix}^{+-}}{dm}}{\sqrt{\frac{dN_{mix}^{++}}{dm} \frac{dN_{mix}^{--}}{dm}}} \quad (36)$$

where, $\frac{dN_{sig}}{dm}$ represents the number of correlated muons at each mass, $\frac{dN_{same}^{**}}{dm}$ represents the number of same-sign muon pairs in the same event (** corresponds to the muon sign), and $\frac{dN_{mix}^{**}}{dm}$ represents the number of muon pairs formed from different events. R is a term to correct for the acceptance difference due to the muon sign. If there is no acceptance difference due to the sign, R = 1. In this analysis, since muon pairs from different events were not reconstructed, R = 1 was used for the calculation.

The result of the combinatorial background subtraction in the dimuon transverse momentum region of ($1 < p_T < 30$) GeV is shown Fig.15.

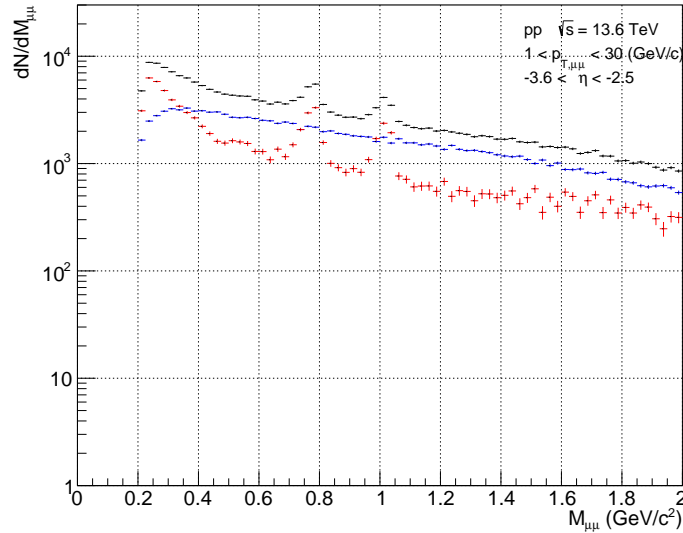
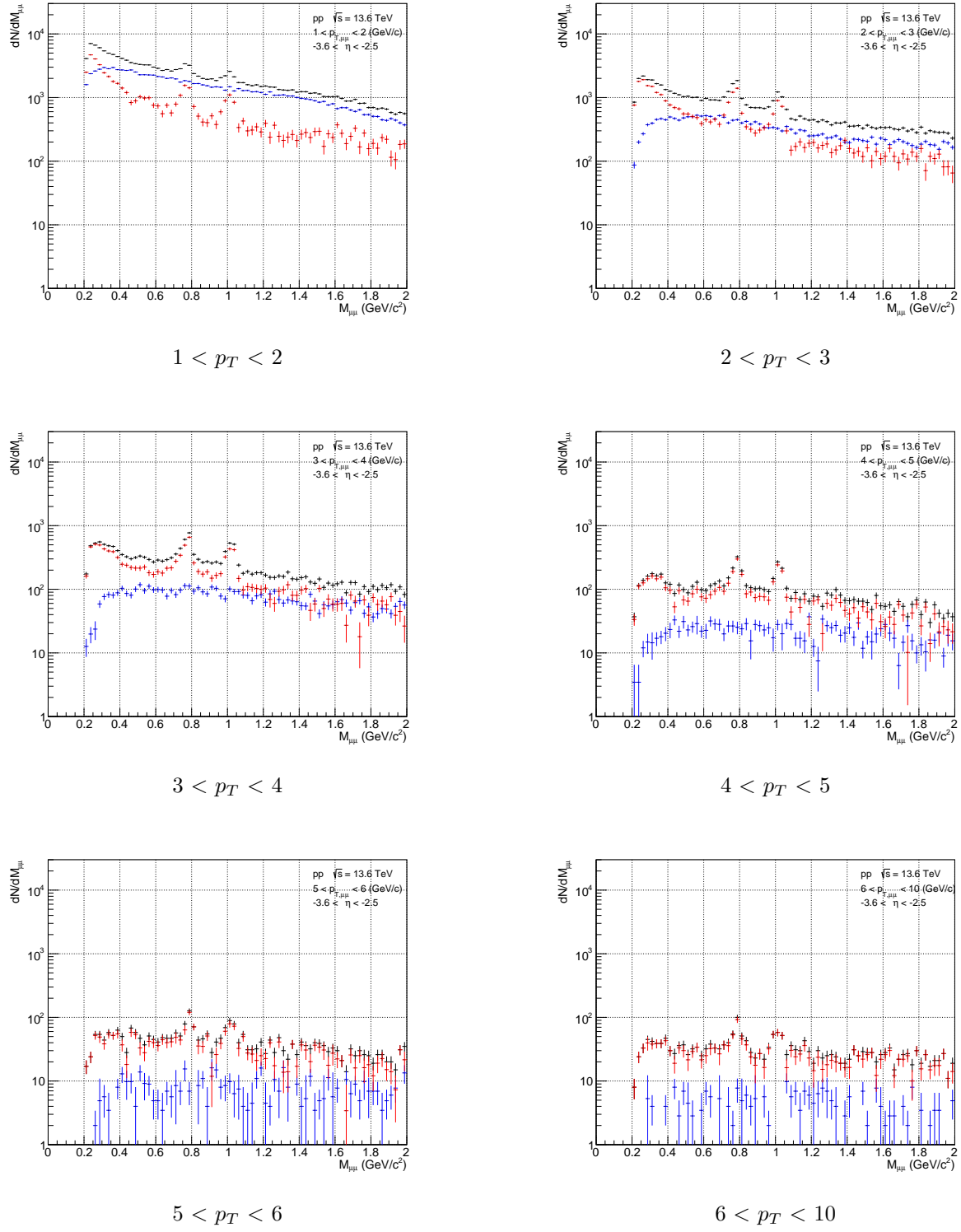


Figure 15: $1 < p_T < 30$

The black distribution represents the invariant mass reconstructed by pairing oppositely charged muon particles from all combinations within the same event, while the blue distribution represents the uncorrelated background events estimated using the Like Sign method. The red distribution, obtained by subtracting the blue from the black one, represents the dimuon invariant mass distribution with correlations. To examine the transverse momentum dependence of the ω and ϕ yields, the mass distributions were separated by dimuon p_T , and uncorrelated background events were subtracted using the Like Sign method in each invariant mass distribution. The subtracted plots are shown in Fig.16.

Figure 16: Result of combinatorial background subtraction of each p_T

In the region of $0 < p_T < 1$ GeV, no peaks for ω and ϕ were observed. This is believed to be due to insufficient resolution of the single muon p_T and the dominance of tracks with incorrect MFT-MCH matching. The region of $6 < p_T < 10$ GeV was chosen to be wider than other transverse momentum regions in order to preserve the statistical significance.

3.5.3 Peak extraction of $\omega \rightarrow \mu\mu, \phi \rightarrow \mu\mu$

The distributions of the correlated dimuon invariant mass obtained from 3.5.2 are used to extract the distributions of $\omega \rightarrow \mu\mu, \phi \rightarrow \mu\mu$. The dimuon invariant mass distribution under $2(GeV/c^2)$ contains pairs of muons coming from light flavor mesons and open heavy flavor. Charm and bottom quarks have heavy masses and are produced through pair creation in the initial collision. The pair-created $c\bar{c}$ quarks separate and form $D\bar{D}$ mesons. The D and \bar{D} mesons undergo semileptonic decays, such as $D \rightarrow \bar{K}^0 + \mu^+ + \nu_\mu$ or $D \rightarrow \mu^+ + \nu_\mu$, and $\bar{D} \rightarrow K^0 + \mu^- + \nu_\mu$ or $\bar{D} \rightarrow \mu^- + \nu_\mu$. Since the parent D and \bar{D} mesons are produced through pair creation, they are strongly correlated, and their decay products, the muons, also exhibit correlation. As a result, the dimuon mass distribution with correlations is included. The same correlation applies in the case of B mesons.

- $\eta \rightarrow \mu^+ \mu^-$
- $\eta \rightarrow \mu^+ \mu^- \gamma$
- $\rho \rightarrow \mu^+ \mu^-$
- $\omega \rightarrow \mu^+ \mu^-$
- $\omega \rightarrow \mu^+ \mu^- \pi^0$
- $\eta' \rightarrow \mu^+ \mu^- \gamma$
- $\phi \rightarrow \mu^+ \mu^-$
- $c\bar{c} \rightarrow D\bar{D} \rightarrow \mu^+ \mu^- + others$
- $b\bar{b} \rightarrow B\bar{B} \rightarrow \mu^+ \mu^- + others$

The decays $\omega \rightarrow \mu\mu$ and $\phi \rightarrow \mu\mu$ are known to exhibit sharp peak structures from previous lepton pair measurements, forming peaks near $0.8 \text{ GeV}/c^2$ and $1.0 \text{ GeV}/c^2$ in the mass distribution. It is known that no sharp peak structures exist for any decays other than the two-body decays of ω and ϕ . Therefore, the continuous component was fitted using an exponential function. The fitting was performed in the range of $0.5 < M_{\mu\mu} < 1.3 \text{ GeV}/c^2$, excluding the regions with peak structures at $0.7 < M_{\mu\mu} < 0.86$ and $0.92 < M_{\mu\mu} < 1.15$. The continuous component was fitted using the exponential function shown (37).

$$f_{BG}(m) = N_0 * \exp\{-p1 * m\} \quad (37)$$

where, N_0 and $p1$ are the fit parameters. The continuous component mass distribution was subtracted using the results from the fit, and Gaussian fits were performed for the ω and ϕ in the mass regions $0.7 < M_{\mu\mu} < 0.86 \text{ GeV}/c^2$ and $0.92 < M_{\mu\mu} < 1.15 \text{ GeV}/c^2$, respectively. The fitting function is given by (38) and (39).

$$f_\omega = N_\omega * \exp\left\{-\frac{1}{2}\left(\frac{m - M_\omega}{\sigma_\omega}\right)^2\right\} \quad (38)$$

$$f_\phi = N_\phi * \exp\left\{-\frac{1}{2}\left(\frac{m - M_\phi}{\sigma_\phi}\right)^2\right\} \quad (39)$$

The fit parameters are $N_\omega, N_\phi, M_\omega, M_\phi, \sigma_\omega, \sigma_\phi$. Specifically, M_ω and M_ϕ correspond to the mean mass positions of ω and ϕ , while σ_ω and σ_ϕ correspond to the mass widths. Using the fit parameters obtained from the continuous component and the Gaussian fits for ω and ϕ , all functions were combined, and a global fit was performed to extract the mean mass positions and mass widths of ω and ϕ . The fit range is $0.5 < M_{\mu\mu} < 1.3 \text{ GeV}/c^2$. The function for the overall fit is given by the (40).

$$f(m) = N_0 * \exp\{-p1 * m\} + N_\omega * \exp\left\{-\frac{1}{2}\left(\frac{m - M_\omega}{\sigma_\omega}\right)^2\right\} + N_\phi * \exp\left\{-\frac{1}{2}\left(\frac{m - M_\phi}{\sigma_\phi}\right)^2\right\} \quad (40)$$

The parameters for the overall fit are similarly $N_0, N_\omega, N_\phi, M_\omega, M_\phi, \sigma_\omega, \sigma_\phi$. The fit results are shown in Figure 17 and Table 1.

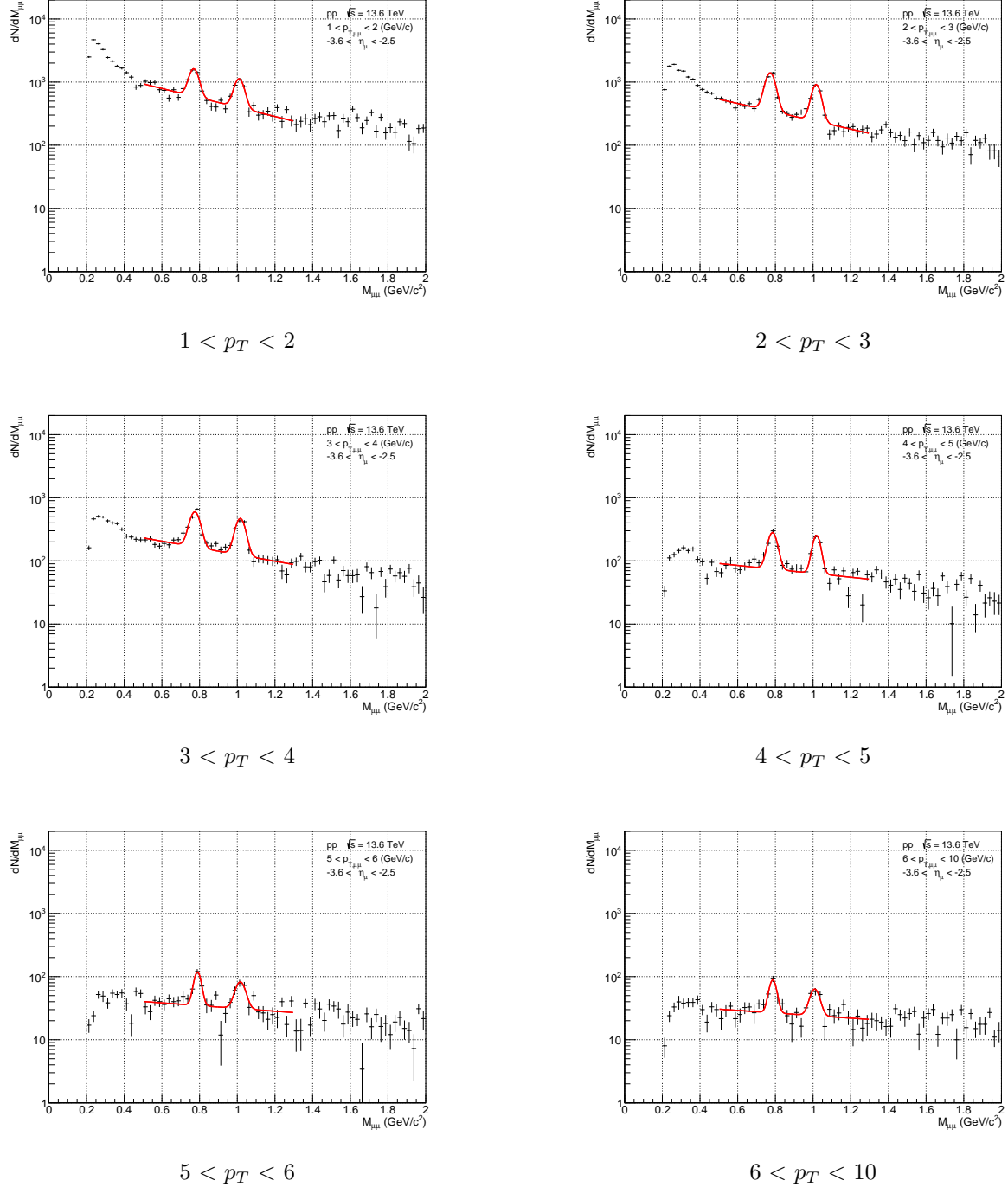


Figure 17: fit result of each p_T

The mean mass positions and mass widths of ω and ϕ for each transverse momentum, as well as the χ^2 of the fit, are summarized in the following table.

3.5.4 Yield calculation of ω, ϕ

Using the mean mass position and mass width of $\omega \rightarrow \mu\mu$ and $\phi \rightarrow \mu\mu$ obtained from the above fit, the yield for each meson was calculated. The number of dimuons falling within 3σ of each Gaussian was

Table 1: Fit Results

	ω mean mass	ω mass width	ϕ mean mass	ϕ mass width	fit χ^2
$1 < p_T < 2$	0.769 ± 0.002	0.025 ± 0.002	1.010 ± 0.002	0.026 ± 0.002	47.74/24
$2 < p_T < 3$	0.773 ± 0.001	0.026 ± 0.001	1.017 ± 0.001	0.024 ± 0.001	58.80/24
$3 < p_T < 4$	0.775 ± 0.002	0.026 ± 0.002	1.016 ± 0.002	0.025 ± 0.002	76.50/24
$4 < p_T < 5$	0.785 ± 0.002	0.024 ± 0.002	1.018 ± 0.002	0.021 ± 0.002	53.96/24
$5 < p_T < 6$	0.789 ± 0.003	0.018 ± 0.003	1.016 ± 0.005	0.026 ± 0.005	36.85/24
$6 < p_T < 10$	0.786 ± 0.003	0.019 ± 0.004	1.009 ± 0.005	0.024 ± 0.003	27.12/24

calculated as the yield for ω and ϕ , respectively.

$$\min = -3 \times \sigma + M \quad (41)$$

$$\max = 3 \times \sigma + M \quad (42)$$

$$\text{Yield} = \sum_{\text{min}}^{\text{max}} F(m) \quad (43)$$

Using the mean mass positions and mass widths of $\omega \rightarrow \mu\mu$ and $\phi \rightarrow \mu\mu$ obtained from the above fit, the yields for each were calculated. The mass distribution, obtained by subtracting the continuous component from the dimuon mass distribution with correlations, was used. For this mass distribution, the number of entries within three times the mass width from the mass positions of ω and ϕ were calculated as their respective yields. The calculation formula is as (43), where the mass distribution after subtracting the continuous component is denoted as $F(m)$. The results from the table above are presented as graphs in

Table 2: Fit Results

	ω Yield	ϕ Yield
$1 < p_T < 2$	$(2.43 \pm 0.18) \times 10^3$	$(1.82 \pm 0.15) \times 10^3$
$2 < p_T < 3$	$(2.79 \pm 0.11) \times 10^3$	$(1.64 \pm 0.09) \times 10^3$
$3 < p_T < 4$	$(1.278 \pm 0.064) \times 10^3$	$(0.886 \pm 0.055) \times 10^3$
$4 < p_T < 5$	$(0.533 \pm 0.038) \times 10^3$	$(0.378 \pm 0.033) \times 10^3$
$5 < p_T < 6$	$(0.159 \pm 0.021) \times 10^3$	$(0.142 \pm 0.023) \times 10^3$
$6 < p_T < 10$	$(0.033 \pm 0.005) \times 10^3$	$(0.023 \pm 0.004) \times 10^3$

36 and 37.

3.6 Analysis for improving MFT-MCH matching purity

The mass distribution of dimuons with p_T below 1 GeV, which is not shown in 16, is presented here. From 18, the peak structures of ω and ϕ could not be measured. This is due to the insufficient reconstruction resolution of η , p_T , and ϕ at low p_T for single muons. The introduction of the MFT is expected to enable high-precision measurements of η and ϕ , which would improve the reconstruction resolution of p_T through enhanced η and ϕ resolution. However, with the current reconstruction method, sufficient resolution has not been achieved, resulting in the inability to observe the peaks of ω and ϕ in the dimuon invariant mass distribution at low transverse momentum. This can likely be attributed to issues in the matching between tracks from the newly introduced MFT and those from the MCH, which prevent achieving adequate resolution. In this chapter, we present an analysis aimed at improving the MFT-MCH matching purity across all transverse momentum distributions, without restricting to low p_T .

3.6.1 MFT-MCH matching χ^2 Optimization

Using the yield analysis method for $\omega \rightarrow \mu\mu, \phi \rightarrow \mu\mu$ described in 3.5.2-??, the MFT-MCH matching χ^2 cut value for single muon tracks was optimized to maximize signal detection efficiency. The MFT-MCH

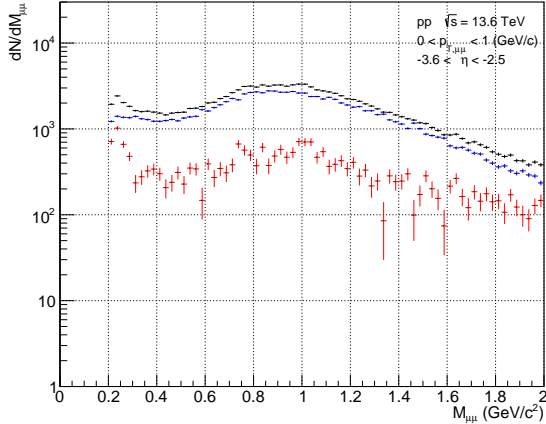


Figure 18: Combinatorial subtraction of dimuon transverse momentum $0 < p_T < 1$

matching χ^2 value represents the difference in parameters when extrapolating MFT and MCH tracks to the matching plane. A larger χ^2 value tends to indicate more fake matches, whereas a smaller value corresponds to more correct matches. By applying a cut on this value, fake match tracks can be removed. however, it is necessary to optimize the cut to minimize fake matches while preserving as many correct matches as possible. In this study, the optimization was performed by maximizing the signal significance using the peaks of ω and ϕ . The signal was calculated by performing the same analysis as in 3.5.2, 3.5.3, and ?? for the mass distributions in all transverse momentum regions. The number of background events was determined by counting the entries in the background-subtracted mass distribution within the same mass window used for signal calculation, and this was used as the background estimate. The significance, $S/\sqrt{S + BG}$, was then calculated. This calculation was performed for mass distributions reconstructed using only muons with an MFT-MCH matching χ^2 below a given threshold. Fig. 19 presents the results of the combinatorial background subtraction after applying the χ^2 cut. Similar to 16, the black histogram represents the mass distribution reconstructed from all oppositely charged muon pairs in the same event, while the blue histogram represents the combinatorial background estimated using the Like Sign method. The red histogram corresponds to the background-subtracted distribution, representing the invariant mass distribution of correlated dimuons.

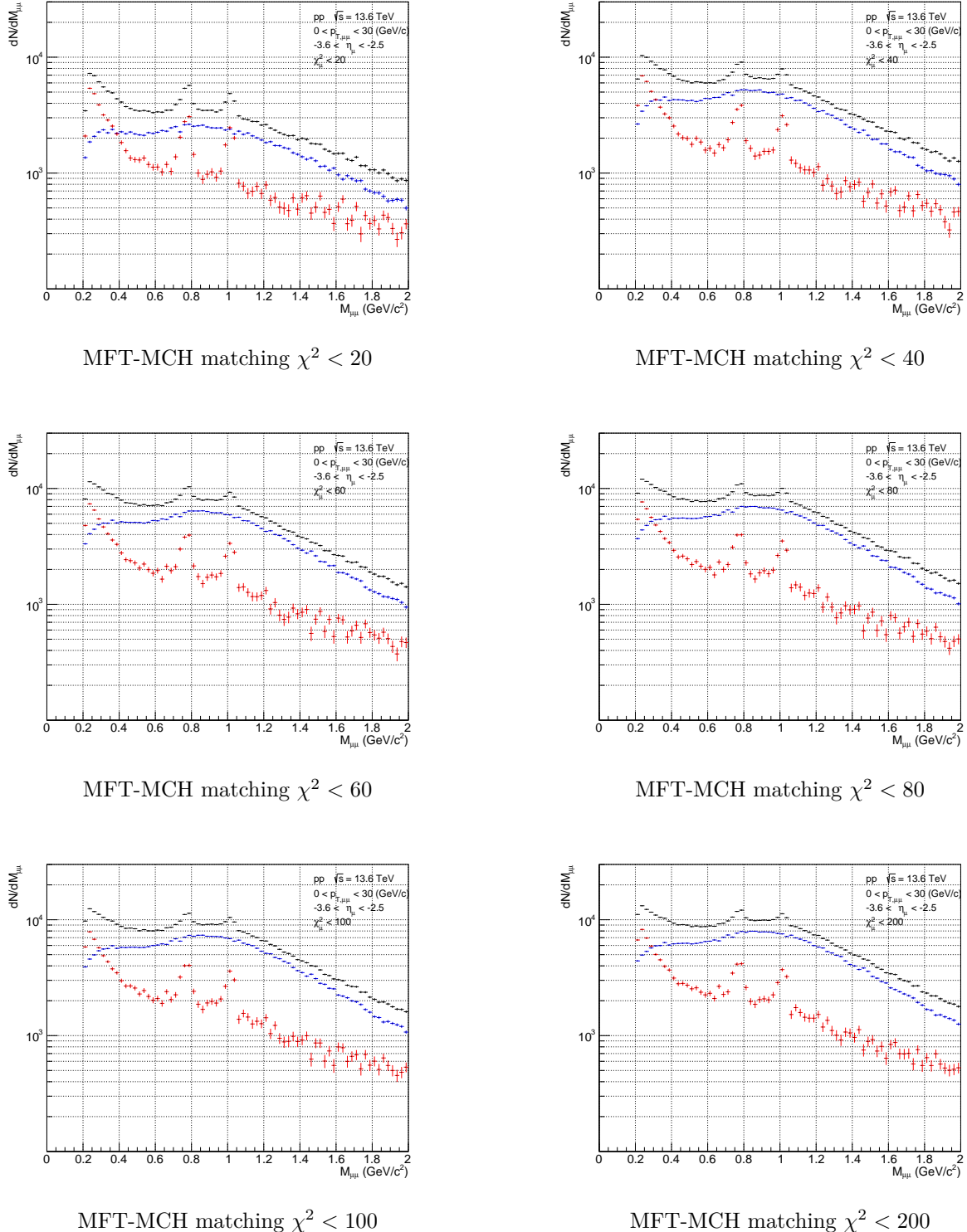
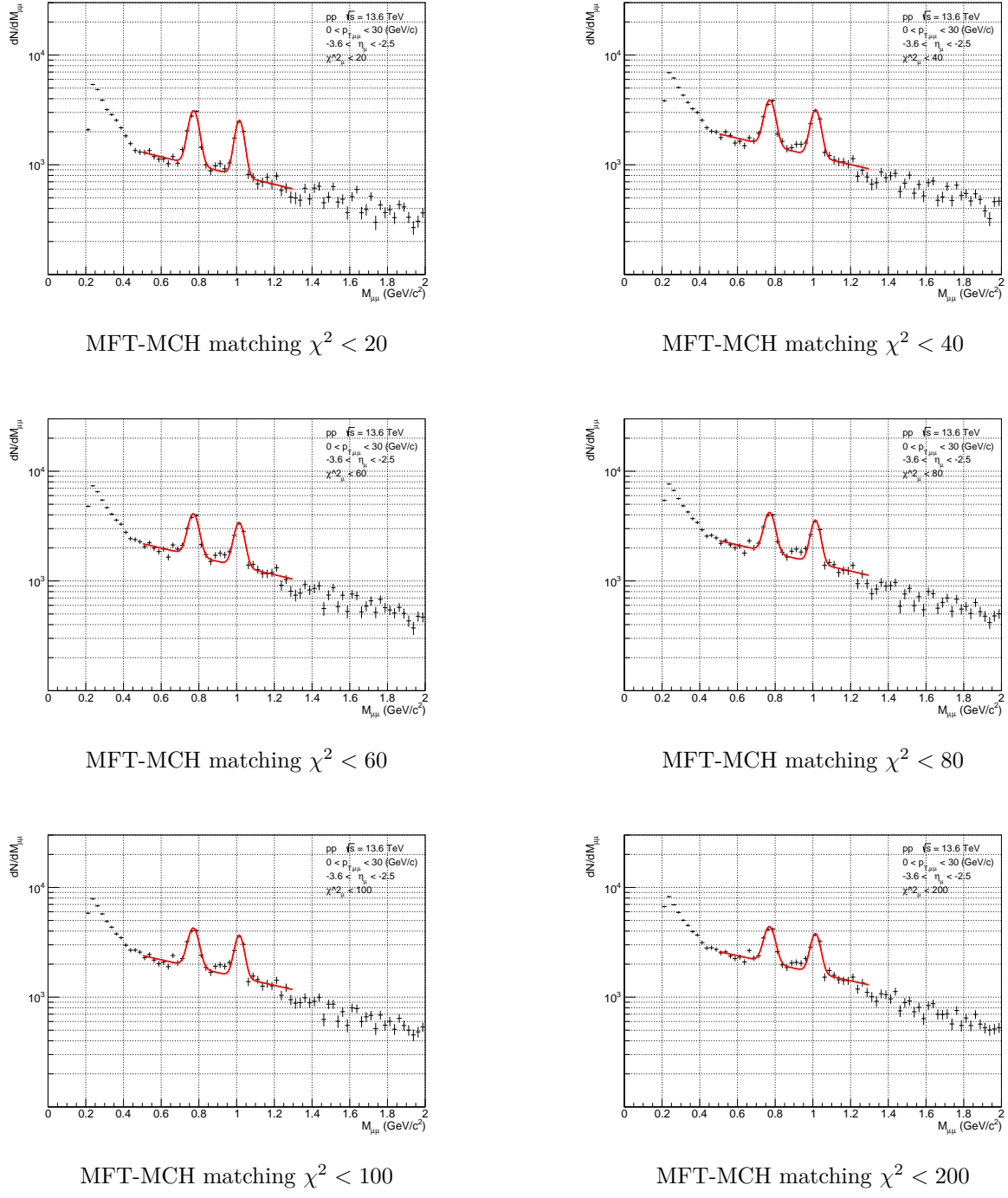


Figure 19: The result of Combinatorial Background subtraction after applying the MFT-MCH matching χ^2 cut

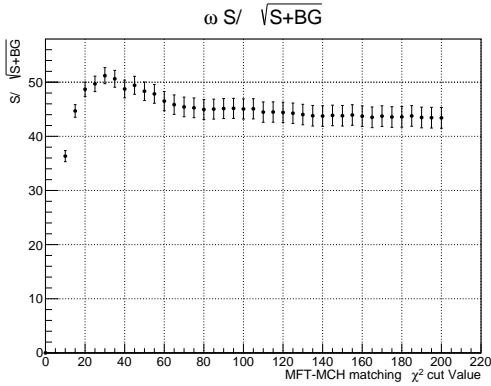
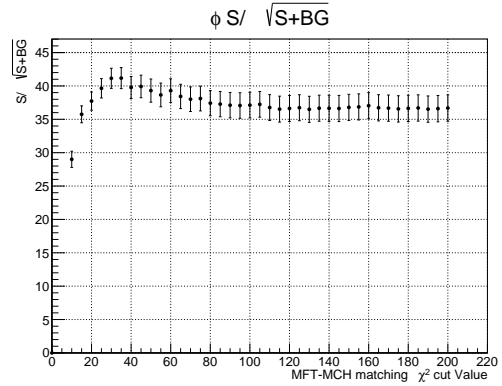
By reducing the χ^2 cut, the black distribution decreases in size. Additionally, it can be observed that the ω and ϕ peaks in the red distribution become more pronounced. The fitting results for this red distribution are shown in the Fig.20.

Figure 20: MFT-MCH matching χ^2

The horizontal axis represents the matching χ^2 , while the vertical axis shows $S/\sqrt{S + BG}$. As the cut value is reduced, the value of $S/\sqrt{S + BG}$ increases. When a cut of $\chi^2 < 30$ is applied, $S/\sqrt{S + BG}$ reaches its maximum for both ω and ϕ . From this result, it is evident that the optimal matching χ^2 value is $\chi^2 < 30$.

3.6.2 Fake Match Track Removal Analysis of MFT-MCH-MID Track using MFT Track η - MCH Track η

The η distribution of Global Tracks differs significantly from the true distribution. This discrepancy arises due to muon reconstruction involving the MFT, indicating issues with MFT-MCH matching. Fake

Figure 21: ω figure of meritFigure 22: ϕ figure of merit

matches contribute to this significantly distorted η distribution. By removing these distortions, it is shown that the resolution of η , p_T , and ϕ for single muons improves. In this analysis, Fake matches are removed by utilizing the difference in η between the MFT Track and MCH Track that constitute the Global Track. The dataset used is LHC24b1, which consists of Monte Carlo data of pp collisions at $\sqrt{s} = 13.6$ TeV from minimum-bias events. This simulation data has been compared with real data, confirming that they exhibit the same behavior.

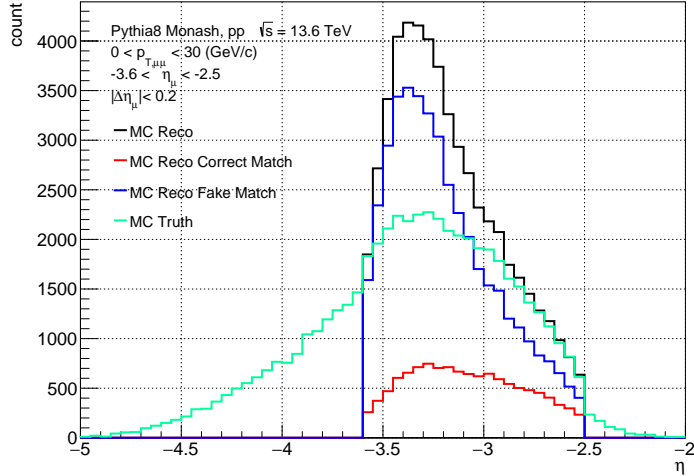
Figure 23: η distribution of Global Track

Figure 23 shows the η distribution of Global Tracks for all p_T regions. The black histogram represents the reconstructed η distribution of Global Tracks. The blue histogram corresponds to the η distribution of reconstructed tracks identified as Fake matches, while the red histogram represents the η distribution of correctly matched tracks. The green histogram represents the true η distribution corresponding to the black reconstructed tracks. Comparing the black reconstructed muon distribution with the green true distribution, the acceptance range of MFT-MCH-MID Tracks is $-3.6 < \eta < -2.5$. However, in the green distribution, muons with η values smaller than -3.6 are reconstructed within the $-3.6 < \eta < -2.5$ range. This phenomenon is likely caused by muons that passed through the absorber and subsequently traversed the MCH-MID system while being outside the MFT acceptance. To remove such tracks, a $\Delta\eta$ cut is applied as (44).

$$\Delta\eta = \text{MFT } \eta - \text{MCH } \eta \quad (44)$$

For each track, $\Delta\eta$ was calculated. Fig.24 shows the distribution. The black represents the distribution of reconstructed muons, the blue represents the distribution of Fake Match tracks, and the red represents the distribution of Correct Match tracks.

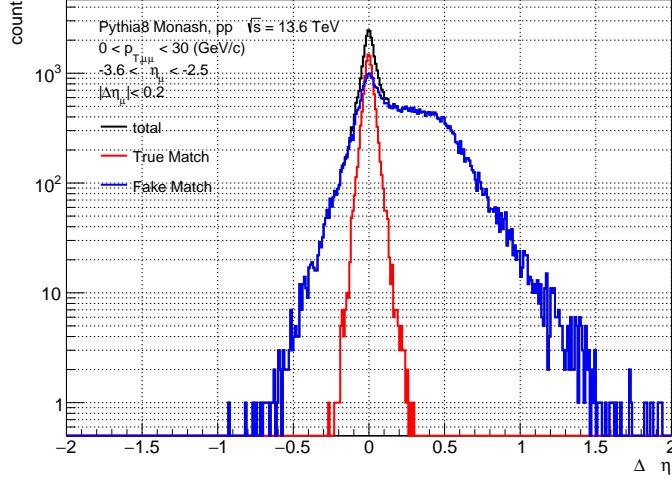


Figure 24: $\Delta\eta$ distribution

For $|\Delta\eta| > 0.2$, Fake Match tracks dominate. By applying a $|\Delta\eta| < 0.2$ cut to remove Fake Matches while retaining as many Correct Matches as possible, the distributions and resolutions of each physical quantity are shown for this case.

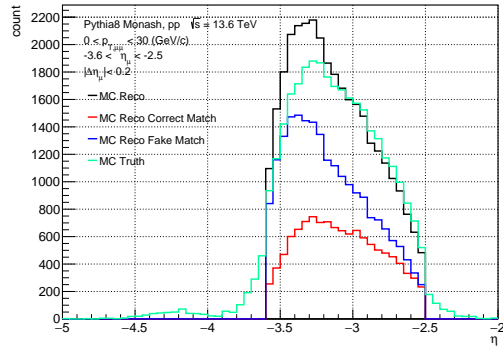


Figure 25: The η distribution of Global Tracks after the $\Delta\eta$ cut

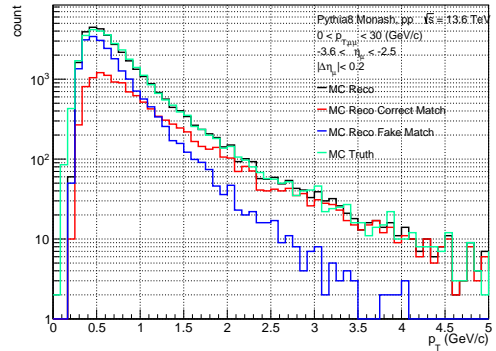
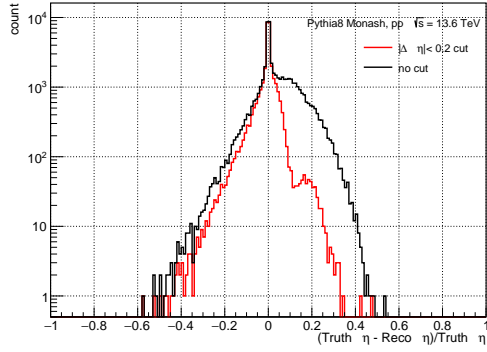
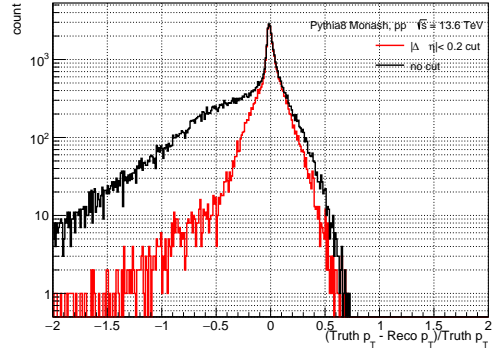
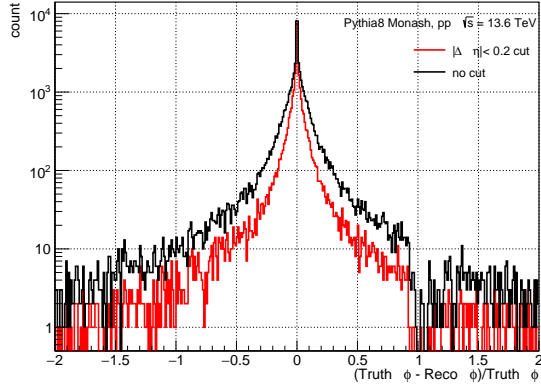
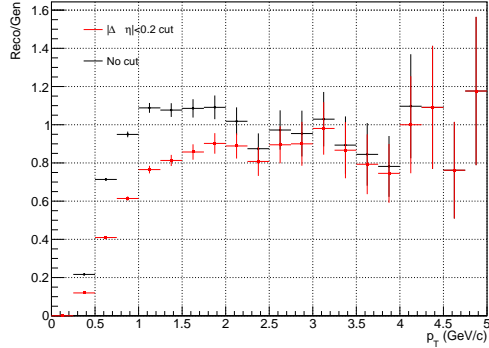
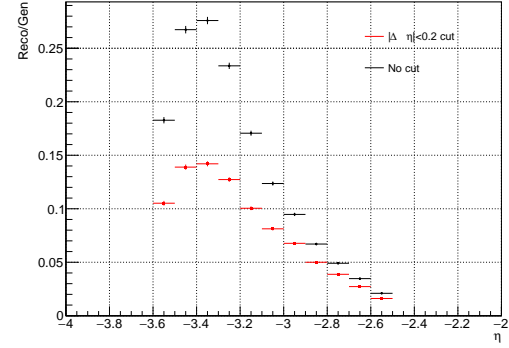
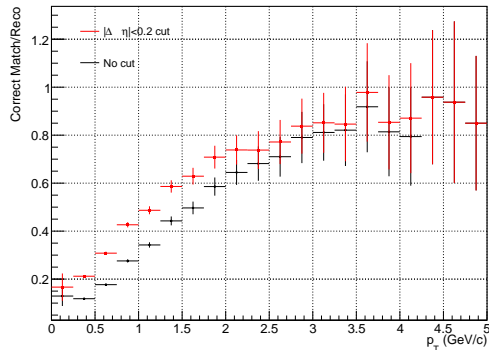
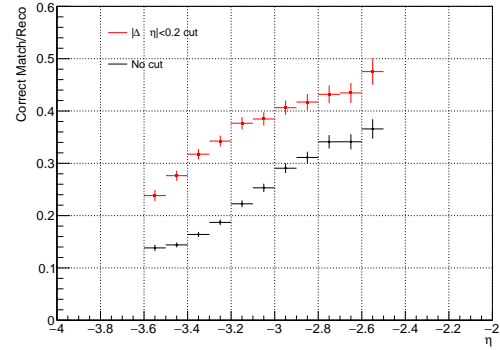
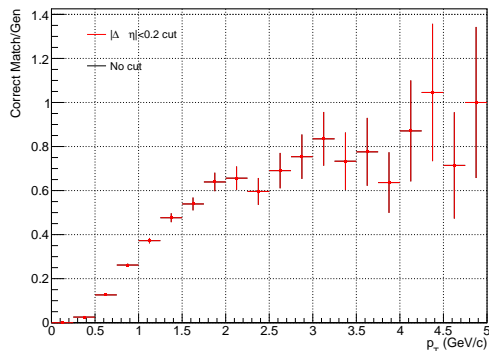
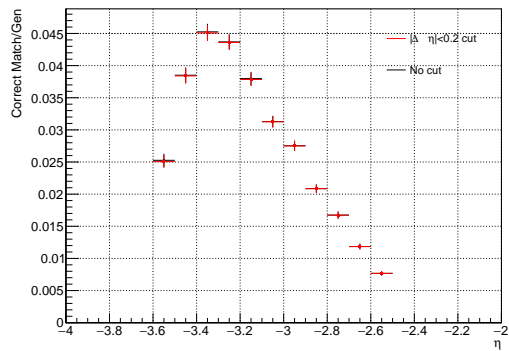


Figure 26: The p_T distribution of Global Tracks after the $\Delta\eta$ cut

Fig.25 shows the η distribution after the $\Delta\eta$ cut. Additionally, Fig.26 displays the p_T distribution after the $\Delta\eta$ cut. As in Figure 23, the black histogram represents all reconstructed muon tracks, the red represents Correct match tracks, and the blue represents Fake Match tracks. The green histogram corresponds to the true η distribution for the black muons. Comparing the green distribution of η after the cut with Figure 23, we see that the muons distributed at $\eta < -3.8$ have been removed. Furthermore, this cut successfully removes a large portion of the Fake match tracks that were present in the range of $-3.6 < \eta < -3.2$. However, as can be seen from Figure 26, Fake matches originating from low transverse momentum still remain.

Figure 27: Resolution of η Figure 28: Resolution of p_T Figure 29: Resolution of ϕ

Figures 27, 28, and 29 show the resolution of p_T , η , and ϕ , respectively. The horizontal axis represents the resolution, which is calculated by subtracting the reconstructed quantity from the true physical quantity and then dividing by the true value. The vertical axis represents the count. The black distribution shows the resolution without applying the $\Delta\eta$ cut, while the red distribution shows the tracks after applying the $|\Delta\eta| < 0.2$ cut. By comparing the black and red histograms, it is clear that the resolution has small value for all distributions. This shows that the resolution improves with the cut. Next, we will describe the efficiency and matching purity improvements due to the cut. The $|\Delta\eta| < 0.2$ cut was applied in such a way as to discard as few correct match tracks as possible, while removing fake match tracks. For the p_T distribution, the efficiency drops below 2 GeV, but the matching purity improves. The product of efficiency \times purity remains unchanged compared to before the cut. This indicates that the cut does not significantly remove correct matches. For the η distribution, efficiency is reduced in the range $-3.6 < \eta < -3$, but matching purity improves in the range $-4 < \eta < -2$. Similarly, the product of efficiency \times purity for η also remains unchanged compared to before the cut.

Figure 30: Efficency of p_T Figure 31: Efficency of η Figure 32: Purity of p_T Figure 33: Purity of η Figure 34: Efficency \times Purity of p_T Figure 35: Efficency \times Purity of η

4 Results and Discussion

In this chapter, the graphs of the ω and ϕ yields calculated in 2 are presented as the conclusion. Figures

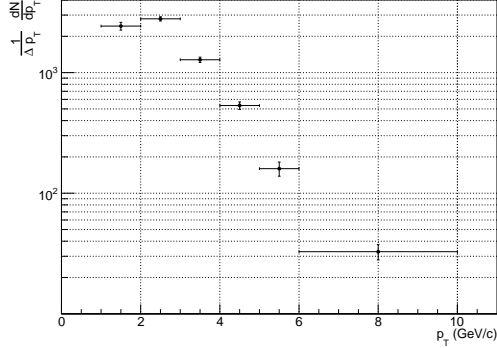


Figure 36: ω yield

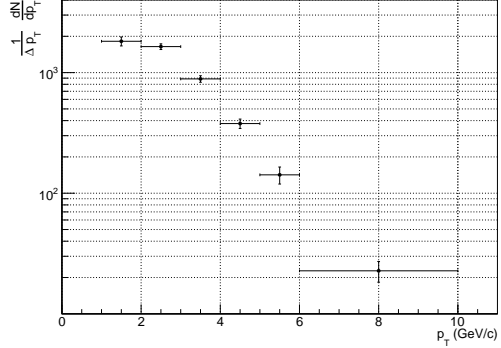


Figure 37: ϕ yield

36 and 37 show the transverse momentum spectra of the production yields of ω and ϕ . The horizontal axis represents the transverse momentum of ω and ϕ , while the vertical axis represents the number of counts. Since these spectra are uncorrected, no physical discussion can be made. However, it is observed that the yields decrease as the transverse momentum increases. This behavior is similar to the p_T spectrum of ϕ production cross-sections measured using forward dimuons in Run 2. Although the p_T spectrum of ω production cross-sections has not been published, the present results exhibit a similar trend to those measured in Run 2. Here, it is necessary to consider the contribution of $\rho \rightarrow \mu\mu$. The ρ meson has a mean mass of $m = 775.26$ MeV and a full width of $\Gamma = 149.1$ MeV, leading to a broader distribution than ω , which is located at a very similar mass position. Given that the signal extraction method used in this analysis accounts for the broad width of the ρ , it is considered that the peak structure of ω is not significantly affected. As a future prospect, improving the resolution of single-muon kinematic variables will enhance the mass resolution, making the ω peak sharper and allowing better separation between the ρ and ω peaks. Additionally, by applying acceptance-efficiency corrections using the forward detector system for $\omega \rightarrow \mu\mu$ and $\phi \rightarrow \mu\mu$ dimuon reconstruction, the integrated luminosity can be determined from the event counts. This will enable the calculation of production cross-sections from the present results, allowing for direct comparison with Run 2 results.

Discuss single muon track reconstruction, 3.6, and future prospects as well. In the current muon track reconstruction algorithm, the pseudorapidity (η) and azimuthal angle (ϕ) of the muon are determined using the MFT standalone track to improve their precision. However, the DCA is calculated using parameters obtained from the global fit of the MFT-MCH-MID track. Since using tracks closer to the collision point allows for more precise measurements unaffected by the absorber, it is expected that the accuracy of the DCA measurement can be improved by using the parameters of the MFT track that constitutes the MFT-MCH-MID track. Furthermore, improvements in MFT-MCH matching are also needed. As seen in 32, the matching purity significantly decreases at low transverse momentum (p_T). This degradation occurs because low- p_T muons undergo multiple scattering and energy loss in the absorber, making MFT-MCH matching more challenging. However, this study demonstrated that applying a $\Delta\eta$ cut improves matching purity in the low- p_T region. This result suggests that continued analysis can further enhance matching purity.

The ultimate goal is to measure the changes in the mass distribution of light vector mesons in lead-lead collision events. This study has revealed several remaining challenges, including issues with matching purity at low transverse momentum and the development of the track reconstruction algorithm. Additionally, improving the quality of muon tracks in high-multiplicity events in heavy-ion collisions is

another challenge. As a first step, efforts will be focused on improving matching purity and developing the track reconstruction algorithm in proton-proton collisions, where the event multiplicity is relatively low. Subsequently, similar improvements will be pursued in heavy-ion collisions. Ultimately, the aim is to clarify the changes in the mass distribution of light vector mesons due to QGP formation and observe the restoration of chiral symmetry.

5 Summary

In this study, we analyzed forward muon pairs in ALICE from $\sqrt{s} = 13.6$ TeV pp collisions. The peaks corresponding to $\omega \rightarrow \mu\mu$ and $\phi \rightarrow \mu\mu$ in the dimuon mass distribution were extracted by fitting them with Gaussian functions, while other components were fitted with an exponential function. These analyses were performed for each transverse momentum range, and the transverse momentum spectra of ω and ϕ yields were presented. Additionally, an analysis was conducted to improve the matching purity between the MFT, introduced in Run 3, and the downstream detectors. By applying a cut on the difference in η between the MFT Track and the MCH Track that constitute the Global Track, we demonstrated the ability to remove Fake Match tracks. Furthermore, the optimal MFT-MCH matching χ^2 cut was determined using the signal yields of ω and ϕ . As a future prospect, further improvements in the quality of Single Muon Tracks will be pursued. Ultimately, this study aims to clarify the changes in the mass distribution of light vector mesons caused by the formation of the QGP in lead-lead nuclear collisions.

6 Acknowledgements

References

- [1] S. Navas *et al.* [Particle Data Group], Phys. Rev. D **110**, no.3, 030001 (2024) doi:10.1103/PhysRevD.110.030001
- [2] W. Weise, Nucl. Phys. A **553**, 59C-72C (1993) doi:10.1016/0375-9474(93)90615-5
- [3] A. Maire, "Phase diagram of QCD matter: Quark-Gluon Plasma," 2015. Available at: <https://cds.cern.ch/record/2025215>
- [4] ALICE Collaboration., Acharya, S., Adamová, D. et al. The ALICE experiment: a journey through QCD. Eur. Phys. J. C 84, 813 (2024). <https://doi.org/10.1140/epjc/s10052-024-12935-y>
- [5] F. Geurts and R. A. Tripolt, Prog. Part. Nucl. Phys. **128**, 104004 (2023) doi:10.1016/j.ppnp.2022.104004 [arXiv:2210.01622 [hep-ph]].
- [6] S. Acharya *et al.* [ALICE], [arXiv:2308.16704 [nucl-ex]].
- [7] R. Rapp and J. Wambach, Adv. Nucl. Phys. **25**, 1 (2000) doi:10.1007/0-306-47101-9_1 [arXiv:hep-ph/9909229 [hep-ph]].
- [8] S. Damjanovic *et al.* [NA60], Nucl. Phys. A **783**, 327-334 (2007) doi:10.1016/j.nuclphysa.2006.11.015 [arXiv:nucl-ex/0701015 [nucl-ex]].
- [9] "Technical Design Report for the Muon Forward Tracker," CERN-LHCC-2015-001, ALICE-TDR-018, 2015. Available at